Contact stiffness of finite size subsurface defects for atomic force microscopy: Three-dimensional finite element modeling and experimental verification

Zehra Parlak and F. Levent Degertekin[a)]
G. W. Woodruff School of Mechanical Engineering, Georgia Institute of Technology, Atlanta, Georgia 30332-0405, USA

We describe a three-dimensional (3D) finite element analysis model of the contact between an atomic force microscopy (AFM) tip and a substrate with finite size subsurface structures. The model can simulate the contact stiffness measured by a scanning AFM tip on the surface of a sample with buried nanoscale structures. In addition to the analytical verification and convergence analysis, we present the results of an experimental verification study. For this purpose, we use an atomic force acoustic microscopy setup and special silicon samples with well defined subsurface cavities fabricated by focused ion beam techniques. The 3D model is also used for parametric analysis of subsurface defect detection, and imaging simulations are performed for practical applications such as AFM imaging of electromigration defects. © *2008 American Institute of Physics.*
[DOI: 10.1063/1.2936881]

I. INTRODUCTION

Atomic force microscopy (AFM) has been initially developed for topography imaging.[1] Nevertheless, several methods, including ultrasonic methods combined with the AFM have made this instrument useful for characterization of mechanical properties of surfaces at the nanoscale while maintaining its nondestructive nature.[2] Several ultrasonic AFM techniques, such as atomic force acoustic microscopy (AFAM),[3–7] ultrasonic force microscopy,[8,9] scanning modulation microscopy,[10] and scanning near-field ultrasound holography,[11] have been developed during the past decade. Most of these techniques use higher flexural or torsional vibration modes of the cantilever which are detected by photodiode while the cantilever tip is in contact with the substrate. The elasticity of this contact is called the contact stiffness which can be represented by a spring constant k^*. Ultrasonic AFM methods can evaluate the contact stiffness by detecting the shifts in flexural and torsional mode resonance frequencies. Since the value of k^* is a function of mechanical properties of the substrate,[12,13] these methods provide the ability for material characterization[14,15] and subsurface imaging.[6,9,16–20] Subsurface imaging by AFM may increase the reliability and repeatability of the fabrication processes used in microelectronic devices and nanoscale structures by detecting defects, such as electromigration voids,[21] and provide more insight on the manufacturing and testing of nanoscale structures buried under a surface.

Interpreting experimental contact stiffness measurements requires adequate analytical or numerical models. For a half-space substrate, the contact theory introduced by Hertz[22] can be used. The contact stiffness between a layered media and the AFM tip can be calculated by using analytical solutions.[23] In addition to these solutions, numerical methods such as finite element analysis (FEA) can evaluate contact stiffness for multilayered media and half-space material.[23,24] In these cases, FEA models have used axisymmetry while evaluating the contact stiffness of the AFM tip-substrate contact. On the other hand, there has not been a validated model for the effects of finite size nanoscale subsurface structures on the contact stiffness. Although some researchers used two-dimensional FEA models previously,[16] these models always assume an axisymmetric geometry that imposes limitations on structures and cannot be used to simulate an imaging scan. A 3D FEA model of AFM contact can quantitatively characterize the effects of various subsurface structures with arbitrary shape and lateral position relative to the AFM tip.

In this paper, we describe a 3D FEA model for the AFM tip-substrate contact, where the substrate can include a buried object or objects, and perform an experimental model validation study. We first perform convergence analysis on a half-space substrate example and verify our model by comparing the results with the Hertzian contact theory. Since the results of the 3D FEA model of AFM tip-substrate contact cannot be verified by an analytical model, AFAM experiments are conducted on samples with well defined buried nanoscale subsurface defects for validation. We then use our model to investigate the effects of the multiple subsurface structures, contact force levels, and subsurface structure material properties. Finally, the efficacy of ultrasonic AFM for electromigration defect detection in fine microelectronic interconnect lines is investigated as an application example.

II. 3D FEA MODEL FOR AFM TIP-SUBSTRATE CONTACT

To perform contact stiffness analysis for an AFM tip scanning over a substrate with a finite size subsurface structure, it is necessary to create a fully 3D FEA model which does not rely on axisymmetry. In analytical or FEA models

---

[a)]Electronic mail: levent.degertekin@me.gatech.edu.

103, 114910-1

TABLE I. Elastic constants of the materials used in the calculations.

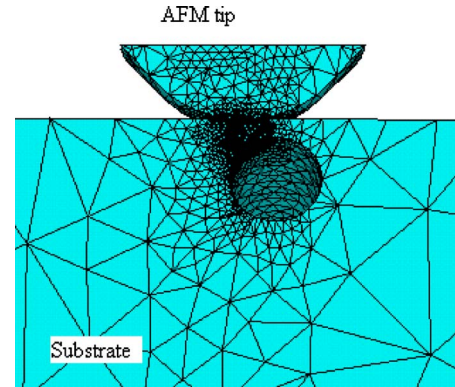| Material	Mechanical Properties	
	Young's modulus (GPa)	Poisson ratio
Silicon	127	0.278
Silicon dioxide	75	0.17
Copper	110	0.33
Tungsten	411	0.28

FIG. 1. (Color online) The computational grid on the Y surface. The volume around the contact is finely meshed until the results converge.

of the AFM tip-substrate contact, the AFM tip is mostly spherical with a 20–200 nm radius. For a spherical tip and half-space sample, researchers use Hertzian contact theory[22] which explains the contact of spherical surfaces.[14,15] Effective Young's modulus E^*, radius of curvature R, and applied force F_0 are the parameters for contact stiffness and contact radius according to this theory.[22] E^* is calculated by using the reduced Young's moduli of the tip M_T and the sample M_S,

$$\frac{1}{E^*} = \frac{1}{M_T} + \frac{1}{M_S}, \tag{2.1}$$

where

$$M_T = \frac{E_T}{1 - \rho_T^2}, \tag{2.2}$$

and

$$M_S = \frac{E_S}{1 - \rho_S^2}, \tag{2.3}$$

where E_S, E_T, ρ_S, and ρ_T are Young's moduli and Poisson ratios of tip and substrate. R is the radius of the AFM tip since the substrate is smooth and has an infinite radius of curvature.

In our 3D FEA model of the AFM tip-substrate contact, M_S is of interest since M_T can be calculated by using mechanical properties of the silicon tip in Table I. Moreover, simulating the AFM tip with its real elastic parameters leads to longer computation time. This issue can be avoided when infinitely rigid tip material is initially assumed in the simulations instead of the actual M_T since in this case the elastic parameters of the tip does not affect the results anymore.[16,24] The effect of the deformation in the AFM tip can later be included analytically to calculate the actual k^* values, as discussed below. For an infinitely stiff tip $(M_T \rightarrow \infty) E^*$ is simply given by M_S according to Eq. (2.1). Consequently, Eq. (2.4) below provides surface stiffness k_S^*, assuming Hertzian contact

$$k_S^* = \frac{3F_0}{2h}, \tag{2.4}$$

where h is the deformation of the substrate.[23]

In order to obtain k^*, three more steps are required. First, M_S is calculated using the following equation:

$$M_S = \sqrt{\frac{k_s^{*3}}{6F_0R}}. \tag{2.5}$$

By substituting M_S of Eq. (2.5) into Eq. (2.1) and using actual M_T, we obtain E^*. Contact stiffness of Hertzian contact can be evaluated using the relation

$$k^* = \sqrt[3]{6F_0RE^{*2}}. \tag{2.6}$$

Please note that the rigid tip method described above does not include the tip deformation in the simulations initially, as would be in standard methods. However, the deformation in the tip is calculated analytically and added later. The accuracy of the method is tested by comparing FEA-based simulations with Hertzian theory for a contact between a spherical silicon tip and substrates with Young's modulus in the 80–400 GPa range. The simulation results are within 0.8% of the analytical calculations over this broad stiffness range, showing the validity of this approach to reduce the computational complexity.

We implement the 3D FEA calculations by ANSYS 11.0.[25] The 3D structural solid element (SOLID92) is used to mesh the tip and the substrate. In addition, we mesh the possible contact area with 3D contact elements (TARGE170, CONTA174). We select the scan direction to be on the x axis and the substrate to be symmetric over the y axis since our ultimate aim is scanning a substrate with a finite size subsurface structure, as shown in Fig. 1. Although the symmetry on the y axis is not necessary, having one more surface in the middle of the geometry provides better meshing. For the cases we are interested in, this simplification is valid. Note that it is always possible for this model to use nonsymmetry condition with more complicated subsurface structures. Spheres, cylinders, or rectangular prisms can be subsurface structures in this y-symmetric model. Also, more than one structure can be present. The tip is spherical and always touches the center of the substrate which is a cylindrical volume with at least 2 μm radius and depth. To simulate a scan over the surface, we move the subsurface structures to different positions and evaluate the contact stiffness for those positions.

One of the drawbacks of the 3D FEA contact model is the computation time which is mainly determined by the nonlinear contact analysis and the number of nodes. The
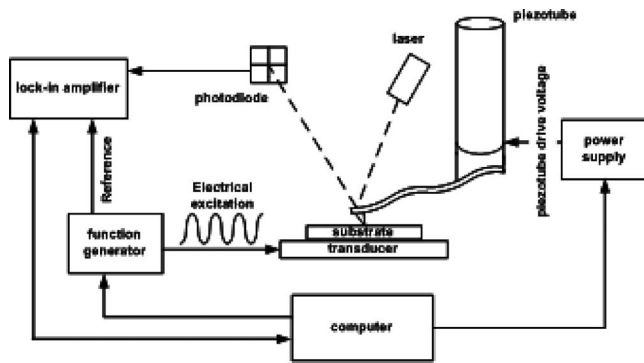
FIG. 2. Schematic of the AFAM setup.

FIG. 3. (Color online) SEM image of the blunted AFM tip used in the experiments.

number of nodes should be high for more accurate results, but a high node number leads to excessive computation time. We use SMRTSIZE command of ANSYS with medium size to control the distribution of the elements on whole volume. This command provides coarse meshing. However, fine meshing around the contact, especially around the contact elements, is necessary. Thus, we refine mesh around the contact more than once for at least 200 nm into the substrate by using NREFINE command. As a result, we obtain a 3D model of AFM tip-substrate contact with an acceptable number of nodes. Each simulation run takes approximately 15 min on average on an Intel P 4 3.0 GHz.

We perform the convergence analysis of the 3D FEA model of the AFM tip-substrate contact for the half-space material since Hertzian contact theory can be used for comparison for this case. We use isotropic material properties used in literature[26] for the half-space material and the silicon tip. According to the convergence analysis, simulated contact stiffness for a half-space converges to values obtained from Hertzian contact theory with less than 1% difference for different materials. Although this result verifies the FEA approach, it does not provide a comparison for simulation of finite size subsurface defects. For this purpose, we conducted AFAM experiments as described below.

III. EXPERIMENTAL VERIFICATION OF 3D FEA MODEL FOR AFM TIP-SUBSTRATE CONTACT

For experimental verification of the 3D FEA contact model, we implemented an AFAM setup and fabricated special samples with smooth surface and well-known subsurface structures.

A. AFAM setup

In AFAM, contact resonance frequency information is converted into the contact stiffness data.[4] Shifts in contact resonance frequencies show the change in mechanical properties of the sample at that point. We modified a commercial AFM system (Dimension 3100, Digital Instruments, Santa Barbara, CA) and implemented AFAM setup, as shown in Fig. 2.[7,15] The substrate is bonded to a piezoelectric transducer which generates out of plane vibrations and has a resonance frequency of 2.3 MHz. While the AFM cantilever is in contact with the substrate surface, a function generator synchronized with the lock-in amplifier excites the piezoelectric
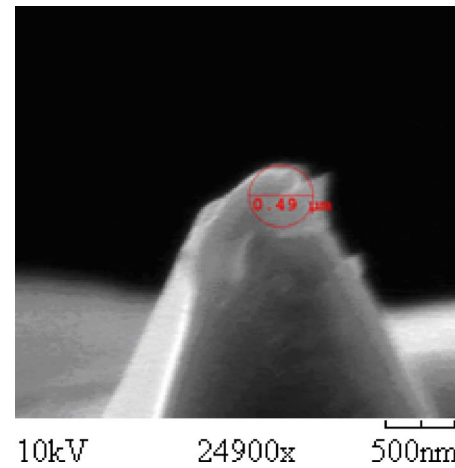
transducer with a sinusoidal voltage which in turn vibrates the sample. The feedback system of AFM keeps the contact force constant; while the vibration of the surface is coupled to the cantilever and the cantilever bending is detected by the bicell detector. The lock-in amplifier measures the rms value and the phase information of the photodiode output at the ultrasonic excitation frequency. At each point of the image, this measurement is repeated for a number of frequencies to obtain the frequency spectrum around a contact resonance and the data are stored in the computer for further processing. The X-Y piezo of the AFM is used to move the cantilever laterally to scan the sample. During the measurements presented in this article, we scan 2.8 μm with 50 data points. Frequency sweep is done by steps of 500 Hz, which causes the stiffness measurement to have 8 N/m steps. MATLAB 7.4 Instrument Control Toolbox is used for programing of instruments and data acquisition.[27]

Contact resonance frequency is a function of the ratio of the contact stiffness and the cantilever stiffness k^*/k_c.[4] Initially, stiff cantilevers seem advantageous to use since they are less affected by adhesive forces as compared to soft cantilevers. The contact resonances of the stiff cantilevers, which can be used for the contact stiffness imaging, are usually at high frequencies. However, at high frequencies, we are limited by the response of the piezotransducer and the photodiode. Because of these limitations, we use CONT40 cantilevers of Veeco. We measured the spring constant as 3 N/m and the free resonance frequency as 42.4 kHz. In addition, we glued the cantilever to the cantilever holder by using ultraviolet (UV) light cured epoxy. This process eliminates unnecessary resonances resulting from holder-cantilever interaction.[28] Although the cantilever has a sharp tip with approximately 10 nm radius before the experiments, we intentionally blunt the tip to avoid further tip shape change during the scan. According to scanning electron microscopy (SEM) image in Fig. 3, the tip has a radius of curvature around 245 nm after blunting. To extract stiffness information from the contact resonance frequency data, we obtain parameters depending on the cantilever dimension and the tip location on the cantilever. Measurements of the resonance frequencies of the free cantilever and resonance frequencies

of the first two flexural modes with surface contact are used for this purpose, and cantilever length and width are obtained from SEM images.[4,7]

B. Sample preparation

In order to experimentally verify our model, we need to fabricate a substrate with well-known subsurface structures in dimensions comparable to the contact radius. With the particular parameters in previous section, the radius of the contact area is less than 20 nm. Regular lithography processes in a clean room allow us to fabricate well-known subsurface structures in micrometer scale with surface topography. This is not desirable for our verification experiments since it may affect the contact stiffness results. To solve this problem, we use a focused ion beam (FIB) (Nova Nanolab 200) system for sample fabrication, following a similar but simpler approach as compared to earlier studies.[9] First, we mount a piece of polished silicon wafer to a SEM holder vertically and image the side by SEM. We mill two alignment marks on a selected area by using FIB. We then mill a cavity of circular cross section between alignment marks, as shown in Fig. 4(a). We are able to mill conical shaped cavities at different dimensions and depths from the surface. The conical cavity used for the experiments here has 500 nm radius at the widest point (base) located under approximately 50 nm silicon and the radius decreases gradually as the cavity gets deeper. We estimate the depth (height of the cone) of this cavity to be around 3 μm based on the measurements on the cross-sectioned samples with similar structures. Thus, the subsurface structure is approximately a cone with 500 nm radius and 3 μm height, as represented in Fig. 4(b). Although topography creation is avoided with this sample fabrication procedure, some particles are unintentionally located around the area of interest. These particles limit the imaging area for contact stiffness measurement. During the experiment, we measured the contact stiffness of three different lines after taking the AFM image of the substrate. These lines are shown with A, B, and C arrows in Fig. 5(a). While line C is scanned as it is shown, lines A and B have offset of 500 nm to avoid the particle on the left side of the Fig. 5(a). The whole topography on these lines is less than 6 nm, as presented by a typical side view in Fig. 5(b). According to the calculations, at these points, holes have radii of 315, 350, and 465 nm while their centers are 550 nm under the surface. Note that these calculations are performed assuming that the cone's long axis is parallel to the polished surface of the silicon sample.

C. Experimental results and comparison with simulation

In the experimental procedure, we first located the area of interest by using tapping mode AFM. We then switched to AFAM mode. First, by varying the contact force and acquiring the frequency data at the same point, we determined the frequency of the third contact mode resonance which is slightly more than 1.21 MHz for 1 μN contact force on silicon surface. We then start the scan on the lines of interest. At each point of the scan, the contact resonance of the can-
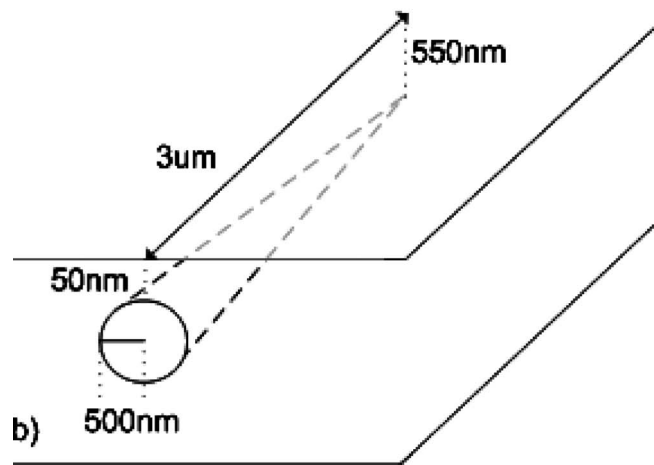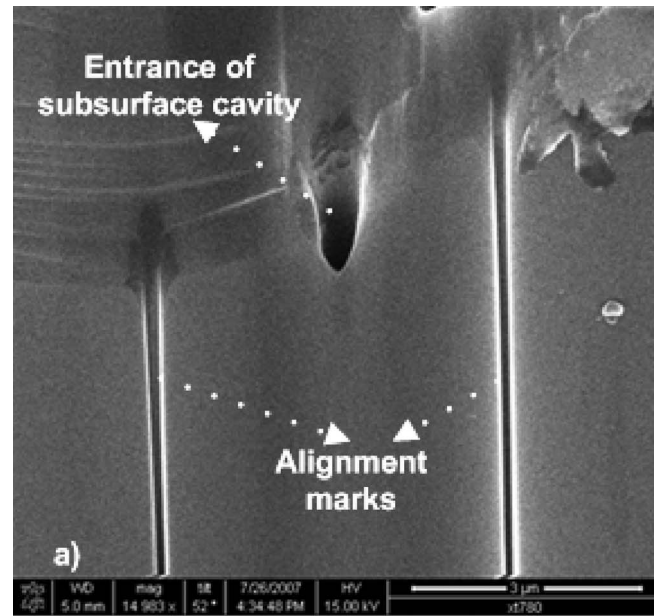

FIG. 4. (a) SEM side view of the substrate used in the experiments. The two lines on the surface are the alignment marks on each side of the conical cavity. (b) Schematic of the subsurface cavity structure.

tilever is measured by sweeping the frequency in a 60 kHz bandwidth around 1.21 MHz. Since the third resonance mode is not affected by the lateral forces as much as the lower modes, the possible effects of lateral forces are ignored in this work.[29] Adhesive forces can be effective in the determination of the contact force especially when the normal force is small.[20] However, in this case, since we apply a significant normal force of 1 μN, we also ignored the effects of possible adhesive forces.

According to the extracted contact stiffness data, the AFM tip and half-space silicon contact has 1702 N/m stiffness for 1 μN contact force. With these values, assuming a spherical tip and the mechanical properties shown in Table I, the tip radius is calculated as 173 nm by Hertzian contact theory assuming a flat silicon surface. Since the SEM image in Fig. 3 shows approximately 245 nm radius of curvature for the tip, we assume that the calculated value is appropriate for further analysis.

The first two image lines (A and B) in Fig. 5(a) are far from the entrance of the cavity. The subsurface structures for
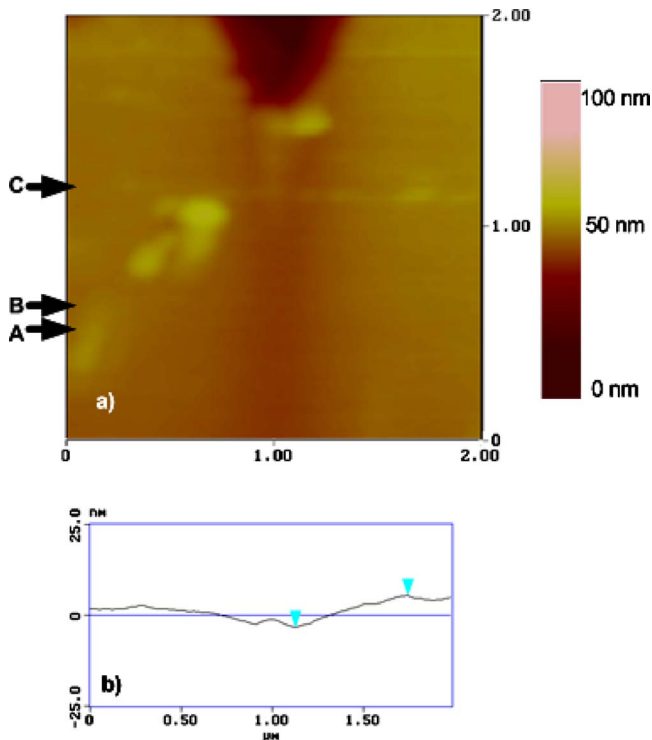
FIG. 5. (Color online) (a) AFM topography image of the substrate. Scan size is 2×2 μm^2. Arrows A, B, and C in (a) represent the lines where the measurements are performed. (b) Cross section of sample surface on line C, showing maximum of 6 nm height difference.

these lines are expected to have approximately 315 and 350 nm radii. On these lines, we tried to capture sections of both clean half-space substrate and the subsurface structure. The experimental and simulated contact stiffness results obtained on these lines are shown in Figs. 6(a) and 6(b). The observed tilt from line A to line B in experimental data can be either a result of shift in lateral piezoposition or the direction of subsurface structure. For the third line, we moved the cantilever tip closer to the entrance of the cavity. At this location, the subsurface cavity has approximately 465 nm radius. This area does not have any disturbances on it, so we centered the subsurface structure in our scan as seen in Fig. 5(a). The experimental and simulated contact stiffness results of line C are presented in Fig. 6(c). For comparison, we plotted the simulation results on the experimental data.

Note that in the FEA simulations, there are no fitting parameters except for the estimated tip radius, cavity radius, and cavity depth. The contact force is measured and silicon material properties (see Table I) are used. Given these conditions, the agreement of the measured and simulated contact stiffness values are in remarkable agreement for all cases. Maximum difference of contact stiffness on bare silicon surface is around 3% for Fig. 6(c). For Fig. 6(a), experiment suggests 1670 N/m contact stiffness at the center of the cavity while simulation gives 1678 N/m for the same point. Also note that, according to the calculations, there is 235 nm of silicon layer over the smallest cavity and this structure is still detectable through the contact stiffness measurement at the surface. In addition, for all cavity radii and depths, the measured maximum change in contact stiffness on the cavity as compared to silicon half-space agrees with the change pre-
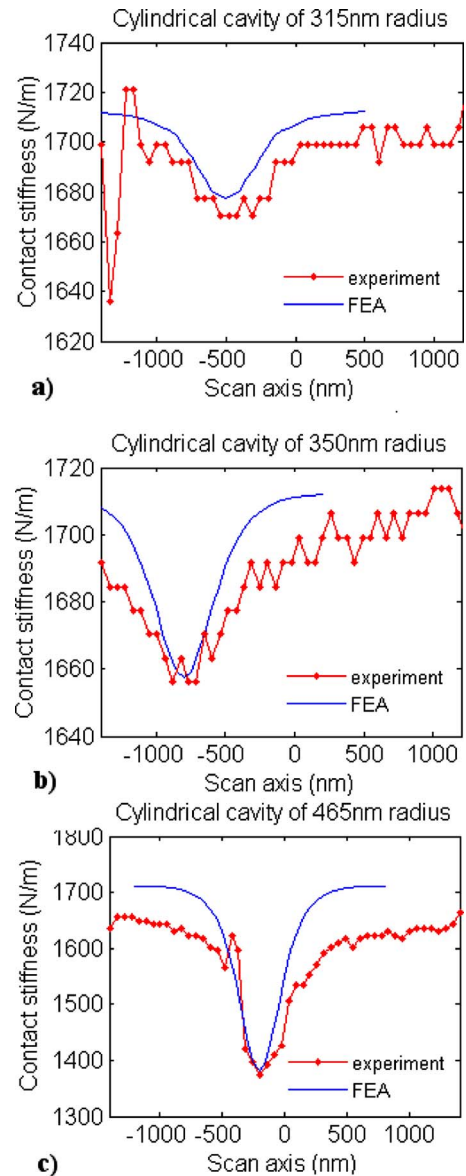

FIG. 6. (Color online) Comparison of experimental and simulation scan data for (a) 315 nm, (b) 350 nm, (c) 465 nm radius of cylindrical cavities.

dicted by simulation. In Figs. 6(b) and 6(c), the simulated contact stiffness changes more rapidly than the experimental results. The reason can be that either the cavities are not perfect as the constant radius cylinders assumed in FEA, or additional thinning on the substrate occurred on these lines, which are closer to the entrance of the cavity. Nevertheless, given the experimental uncertainties and possible errors, these results justify the use of the 3D model for analyzing other types of defects and subsurface structures on the AFM tip-substrate contact.

IV. APPLICATION OF THE MODEL AND DISCUSSION

In this section, the 3D FEA model is used to predict the effects of several defect geometries, elastic properties, as well as imaging parameters such as contact force on ultrasonic AFM. In addition, since this model can evaluate the effects on the contact stiffness caused by multiple subsurface structures with more complex geometries, we investigate the
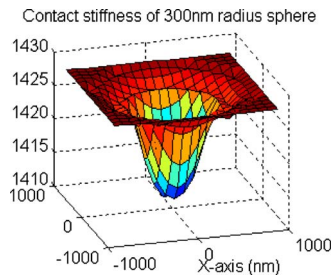
FIG. 7. (Color online) The contact stiffness of a surface with a spherical subsurface cavity which has 300 nm radius. The center of the cavity is 500 nm under the surface.

resolving power of ultrasonic AFM for certain types of defects. We also give practical examples of subsurface defects such as electromigration voids in microelectronic interconnects.

A. Imaging simulation of finite size cavities

One of the advantages of the 3D model of the contact is the capability of the scanning simulation. To demonstrate this capability, we simulate the effects of a spherical cavity on the contact stiffness for a surface scan. The cavity under investigation has 300 nm radius and the center is 500 nm under the silicon surface. We use 1 μN of contact force and 100 nm tip radius during the scan. Contact stiffness distribution on the surface of this case is shown in Fig. 7. Silicon half-space causes contact stiffness of 1427 N/m in the simulations for the given parameters. The lowest contact stiffness resulted by this spherical cavity is 1411 N/m, while an infinitely long cylinder with the same radius and depth has 1395 N/m of contact stiffness on the softest spot. According to experimental data, the particular AFAM setup we developed can detect 10 N/m or more of contact stiffness change. Thus, minimum detectable contact stiffness change Δk is 10 N/m. If we analyze the simulation with this information, we can conclude that a spherical cavity with the given dimensions is barely detectable by our AFAM setup.

The 3D contact model also provides information on the effects of the multiple subsurface structures. As an example, we simulated two cylindrical subsurface cavities in silicon substrate using 100 nm radius tip and 1 μN contact force. Both of these cavities are infinitely long and their height axis is parallel to the surface while their radius is 300 nm. The centers are 500 nm under the surface, as depicted in Fig. 8(b), and the distance between the centers of the cylinders is varied between 800 nm and 1.2 μm. According to the simulation results in Fig. 8(a), the distance between the centers of the cylinders should be more than 1.2 μm so that the subsurface structures can be modeled as independent objects. Note that it is difficult to define a general rule for lateral and depth resolution since the distribution of the contact stiffness is a function of depth, width, and material of the subsurface structure as well as the force and tip radius.

B. Effects of force levels and elastic properties

The tip radius and tip material have significant effect on the lateral resolution and depth in ultrasonic AFM
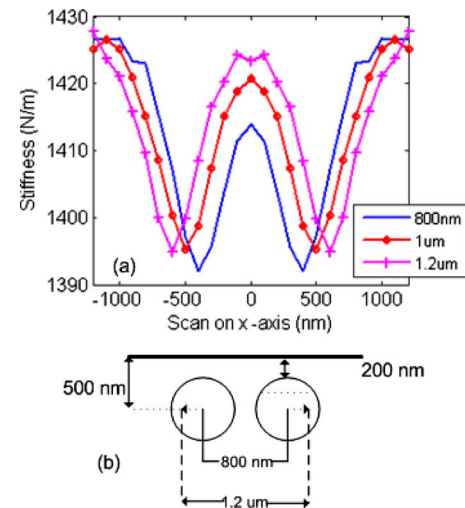

FIG. 8. (Color online) (a) The calculated contact stiffness of silicon substrate with two cylindrical cavities. (b) Schematic of two cylindrical cavities. Their radius is 300 nm and center is 500 nm under the surface. The distance between the centers of the cylinders is varied for the calculations.

applications.[9] However, the observed effects of subsurface structures on the contact stiffness depend on many other variables, such as contact force, material properties of the substrate, and the properties and shape of the subsurface structure. Because of this, we examine the effects of one variable while keeping the rest of them constant. We first investigate how different force levels change the contrast of the contact stiffness image. For this purpose, we apply 200 nN, 1 μN, and 2 μN forces to the geometry depicted in Fig. 8(b) with 800 nm distance between centers. Figure 9 shows the normalized contact stiffness (k^*/k_{Si}^*) results for this geometry, where k_{Si}^* for each curve is the contact stiffness of silicon half-space for that particular applied contact force level. When 200 nN of force is applied, normalized contact stiffness changes by 1.5% (12.5 N/m for $k_{Si}^*=835$ N/m) as the tip scans over the cylindrical cavities. Thus, for example, these defects would barely be detectable in our AFAM setup with 200 nN force assuming a minimum detectable Δk of 10 N/m. Higher forces provide better lateral resolution and contrast because penetration depth is increased to the cylindrical cavities. However, one should optimize the force carefully depending on the substrate and detection system since higher forces can be destructive while providing better subsurface images.
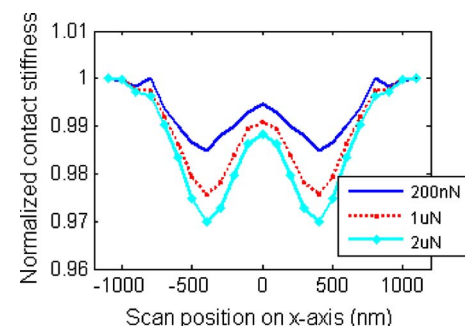

FIG. 9. (Color online) The normalized contact stiffness of the substrate with two cylindrical cavities with different forces. Both of the cavities have 300 nm radius, the distance between their center is 800 nm and they are under 200 nm of silicon.
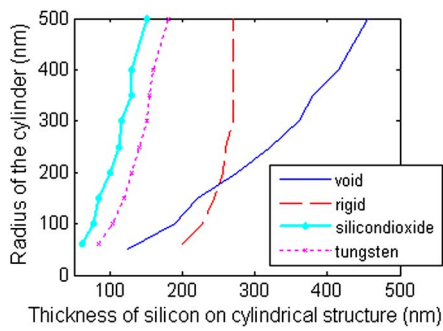
Figure 10

FIG. 10. (Color online) The detection limit contours for the cylindrical defects in silicon substrate. Each contour represents a different defect material.

Second, we investigate the effects of the size and elastic properties on the defect detection limits. For this purpose, we simulate long cylindrical inclusions in silicon made of SiO_2 and tungsten as practical materials (see Table I). To simulate limiting cases, we also generate the results for a cylindrical cavity or a perfectly rigid inclusion of the same shape. We use 1 μN contact force and 100 nm tip radius. As mentioned before, the minimum detectable contact stiffness change Δk of 10 N/m is calculated for our system. In Fig. 10, we plot the minimum defect size and depth required for the detection of these subsurface defects. Each line shows the depth and radius of the corresponding inclusion that result in Δk of 10 N/m in contact stiffness. For each material, the region to left of the contours shows the detectable range of cylindrical defect radius and depth. According to Fig. 10, when there is higher contrast between substrate and structure, smaller inclusions can be detected. As expected, subsurface structures with mechanical properties with large contrast as compared to silicon can be detected easier at larger depths. Consequently, the lines corresponding to the rigid structure and void defects are the rightmost curves. Similarly, tungsten inclusion generates more contrast than a similar silicon dioxide structure. Rigid inclusions can be detected easier than the voids of similar size when they are close to the surface. The steep increase in detectable rigid cylinder radius shows that the penetration depth for this type of defects is limited to about 280 nm regardless of its size for this particular tip radius, tip and substrate material. In contrast, a void located deeper in the substrate can still be detected if it has large enough diameter. Note that although the results in this figure are valid for this particular example, they can serve as a guideline for subsurface detection.

C. A practical example: Formation of electromigration void

Electromigration in interconnects is one of the challenges for reliability of integrated circuits. To understand the formation mechanism of electromigration defects, researchers commonly use x-ray[30,31] or FIB imaging.[21,32] While the spot size of x ray creates resolution problems, using FIB is destructive; hence, it does not allow *in situ* imaging. There-
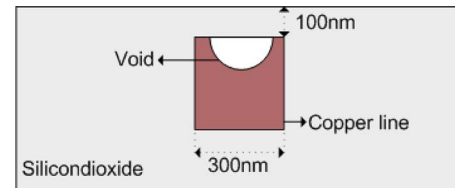

FIG. 11. (Color online) The geometry of the simulated electromigration defect.

fore, we investigate subsurface imaging by AFM as a tool for *in situ* observation of electromigration voids.

For these calculations, we simulate copper (Cu) lines with 300 nm square cross section embedded under 100 nm of SiO_2. X-ray techniques would have difficulty in detecting electromigration voids on 300 nm lines because of the larger spot size. However, AFM may provide better lateral resolution by making use of the small contact radius. To model the formation of the electromigration defects, we place a half-spherical void on the upper side of the Cu line, as depicted in Fig. 11. Then, contact stiffness on the surface is calculated for different radii of half-spherical cavity, simulating the growth of a void. In addition, same calculation is done for Cu line with a rectangular electromigration defect with a base of 300×300 nm^2 and which completely breaks the electrical connection resulting in what is called a fatal defect. All calculations are done by assuming 100 nm of tip radius and 1 μN of force. The results are presented in Fig. 12. As shown in Table I, Cu is slightly stiffer than SiO_2. Since these two materials do not have much contrast in their elastic properties, scan on flawless Cu line indicates a slight (4 N/m) increase in stiffness. With the electromigration void in the Cu line a reduction in contact stiffness is observed depending on the size of the defect. If the void has 50 nm radius, the reduction is about 6 N/m. The slight increase in contact stiffness on either side of the 50 nm radius void is the result of having the stiffer Cu layer under the SiO_2 layer. When the radius of the defect becomes 70 nm, simulation shows 18 N/m of contact stiffness change, which would be detectable with our current setup. More contrast on contact stiffness results as the defect is enlarged. The stiffness change is 65 N/m for the fatal defect case, when the diameter of the void reaches to the width of the line.

The results show that ultrasonic AFM is expected to provide better performance than x ray during the electromigra-
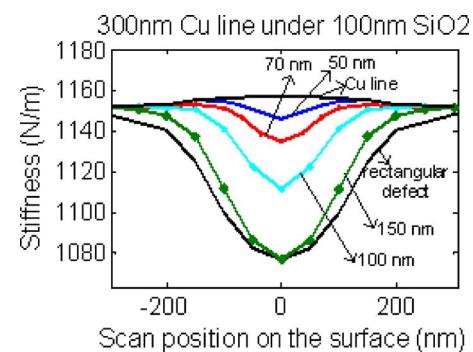

FIG. 12. (Color online) The calculated contact stiffness on a Cu interconnect line with a electromigration defect.

tion void monitoring in thin Cu lines. One of the shortcomings of ultrasonic AFM is the low penetration depth of the method. Although higher forces will provide increase in the penetration depth, it may be destructive. Therefore, the material on the interconnect lines may need to be thinned down to about 100 nm. In addition, ultrasonic AFM cannot be used to detect electromigration defects under a via, since the necessary via height causes the defect area to be far from the AFM probe.

V. CONCLUSION

We developed a 3D FEA model for the AFM tip-substrate contact to examine the effects of finite size subsurface structures on contact stiffness. We verified the model analytically for half-space substrates and performed convergence analysis. For further verification of the model, we fabricated samples with well-controlled nanometer size subsurface structures and carried out AFAM experiments. The agreement between the experiments and simulation results shows that the 3D model can be used to simulate subsurface imaging by AFM on substrates with single and multiple subsurface structures. Using this model, we investigated the effects of the different force levels and elastic properties on the resolution of ultrasonic AFM images. The force study shows that high forces are crucial for sensitive subsurface imaging and the results can be used to determine the optimum force levels for nondestructive operation. We presented a guideline for the detection of subsurface inclusions made of the different materials. Although the results may vary for different forces, substrates, and tip radii, some general conclusions could be drawn. When substrate has high contrast with the buried object in terms of elastic properties, detection of deeper or smaller defects is possible as expected. We also simulated a real life problem, formation of electromigration defects in thin electrical interconnects, as a possible application of subsurface imaging by AFM. The simulation results showed that an electromigration defect can be observed in its early stages using ultrasonic AFM. Better resolution can be achieved if more force is applied or thinner insulator is used. Given the generality of the 3D model presented here, we expect this approach to be used for various applications where AFM is used for mechanical measurements on a substrate with subsurface structures.

ACKNOWLEDGMENTS

[1] G. Binnig, C. F. Quate, and C. Gerber, Phys. Rev. Lett. **56**, 930 (1986).

[2] B. D. Huey, Annu. Rev. Mater. Res. **37**, 351 (2007).

[3] D. C. Hurley, M. Kopycinska-Müller, A. B. Kos, and R. H. Geiss, Adv. Eng. Mater. **7**, 713 (2005).

[4] U. Rabe, K. Janser, and W. Arnold, Rev. Sci. Instrum. **67**, 3281 (1996).

[5] U. Rabe, S. Amelio, M. Kopycinska, S. Hirsekorn, M. Kempf, M. Göken, and W. Arnold, Surf. Interface Anal. **33**, 65 (2002).

[6] D. C. Hurley, K. Shen, N. M. Jennett, and J. A. Turner, J. Appl. Phys. **94**, 2347 (2003).

[7] U. Rabe, S. Amelio, E. Kester, V. Scherer, S. Hirsekorn, and W. Arnold, Ultrasonics **38**, 430 (2000).

[8] K. Yamanaka, H. Ogiso, and O. Kolosov, Appl. Phys. Lett. **64**, 178 (1994).

[9] H. Geisler, M. Hoehn, M. Rambach, M. A. Meyer, E. Zschech, M. Mertig, A. Romanov, M. Bobeth, W. Pompe, and R. E. Geer, *Microscopy of Semiconducting Materials*, Institute of Physics Conference Series No. 169 (IOP, Bristol, UK, 2001), pp. 527–530.

[10] B. C. P. Vairac, Surf. Interface Anal. **27**, 588 (1999).

[11] G. S. Shekhawat and V. P. Dravid, Science **310**, 89 (2005).

[12] K. Yamanaka, A. Noguchi, T. Tsuji, T. Koike, and T. Goto, Surf. Interface Anal. **27**, 600 (1999).

[13] J. A. Turner, S. Hirsekorn, U. Rabe, and W. Arnold, J. Appl. Phys. **82**, 966 (1997).

[14] U. Rabe, S. Amelio, M. Kopycinska, S. Hirsekorn, M. Kempf, M. Goken, and W. Arnold, Surf. Interface Anal. **33**, 65 (2002).

[15] S. Amelio, A. V. Goldade, U. Rabe, V. Scherer, B. Bhushan, and W. Arnold, Thin Solid Films **392**, 75 (2001).

[16] T. Tsuji and K. Yamanaka, Nanotechnology **12**, 301 (2001).

[17] K. B. Crozier, G. G. Yaralioglu, F. L. Degertekin, J. D. Adams, S. C. Minne, and C. F. Quate, Appl. Phys. Lett. **76**, 1950 (2000).

[18] D. C. Hurley, M. Kopycinska-Muller, E. D. Langlois, A. B. Kos, and N. Barbosa, Appl. Phys. Lett. **89**, 021911 (2006).

[19] A. P. McGuigan, B. D. Huey, G. A. D. Briggs, O. V. Kolosov, Y. Tsukahara, and M. Yanaka, Appl. Phys. Lett. **80**, 1180 (2002).

[20] F. Dinelli, M. R. Castell, D. A. Ritchie, N. J. Mason, G. A. D. Briggs, and O. V. Kolosov, Philos. Mag. A **80**, 2299 (2000).

[21] A. V. Vairagar, S. G. Mhaisalkar, A. Krishnamoorthy, K. N. Tu, A. M. Gusak, M. A. Meyer, and E. Zschech, Appl. Phys. Lett. **85**, 2502 (2004).

[22] K. L. Johnson, *Contact Mechanics* (Cambridge University Press, Cambridge, 1985).

[23] G. G. Yaralioglu, F. L. Degertekin, K. B. Crozier, and C. F. Quate, J. Appl. Phys. **87**, 7491 (2000).

[24] G. S. Batog, A. S. Baturin, V. S. Bormashov, and E. P. Sheshin, Tech. Phys. **51**, 1084 (2006).

[25] ANSYS, Inc., Southpointe, 275 Technology Drive, Canonsburg, PA 15317.

[26] L. Gan, B. Ben-Nissan, and A. Ben-David, Thin Solid Films **290–291**, 362 (1996).

[27] The MathWorks Inc., 3 Apple Hill Drive, Natick, MA 01760-2098.

[28] U. Rabe, S. Hirsekorn, M. Reinstädtler, T. Sulzbach, C. Lehrer, and W. Arnold, Nanotechnology **18**, 044008 (2007).

[29] U. Rabe, J. Turner, and W. Arnold, Appl. Phys. A: Mater. Sci. Process. **66**, S277 (1998).

[30] X. Su, C. Stagarescu, G. Xu, D. E. Eastman, I. McNulty, S. P. Frigo, Y. Wang, C. C. Retsch, I. C. Noyan, and C. K. Hu, Appl. Phys. Lett. **77**, 3465 (2000).

[31] G. Xu, D. E. Eastman, B. Lai, Z. Cai, I. McNulty, S. Frigo, I. C. Noyan, and C. K. Hu, J. Appl. Phys. **94**, 6040 (2003).

[32] M. A. Hussein and H. Jun, IEEE Trans. Semicond. Manuf. **18**, 69 (2005).